JACS
JOURNAL OF THE AMERICAN CHEMICAL SOCIETY
Article
pubs.acs.org/JACS

Reduced Graphene Oxide Conjugated Cu_2O Nanowire Mesocrystals for High-Performance NO_2 Gas Sensor

Suzi Deng,[†] Verawati Tjoa,[‡,∥] Hai Ming Fan,*[,§,#] Hui Ru Tan,[⊥] Dean C. Sayle,[¶] Malini Olivo,[#] Subodh Mhaisalkar,[‡] Jun Wei,[∥] and Chorng Haur Sow*[,†]

[†]Department of Physics, National University of Singapore, 2 Science Drive 3, Singapore 117542

[‡]School of Materials Science and Engineering, Nanyang Technological University, 639798 Singapore

[§]Shaanxi Key Laboratory of Degradable Biomedical Materials, School of Chemical Engineering, Northwest University, Xi'an, Shaanxi 710069, China

[⊥]Institute of Materials Research and Engineering, A*STAR (Agency for Science, Technology and Research), 3 Research Link, 117602, Singapore

[¶]Department of Engineering and Applied Science, Cranfield University, Defence Academy of the United Kingdom, Shrivenham SN6 8LA, United Kingdom

[#]School of Physics, National University of Ireland Galway, Galway, Ireland

[∥]Singapore Institute of Manufacturing Technology, 638075, Singapore

Supporting Information

ABSTRACT: Reduced graphene oxide (rGO)-conjugated Cu_2O nanowire mesocrystals were formed by nonclassical crystallization in the presence of GO and *o*-anisidine under hydrothermal conditions. The resultant mesocrystals are comprised of highly anisotropic nanowires as building blocks and possess a distinct octahedral morphology with eight {111} equivalent crystal faces. The mechanisms underlying the sequential formation of the mesocrystals are as follows: first, GO-promoted agglomeration of amorphous spherical Cu_2O nanoparticles at the initial stage, leading to the transition of growth mechanism from conventional ion-by-ion growth to particle-mediated crystallization; second, the evolution of the amorphous microspheres into hierarchical structure, and finally to nanowire mesocrystals through mesoscale transformation, where Ostwald ripening is responsible for the growth of the nanowire building blocks; third, large-scale self-organization of the mesocrystals and the reduction of GO (at high GO concentration) occur simultaneously, resulting in an integrated hybrid architecture where porous three-dimensional (3D) framework structures interspersed among two-dimensional (2D) rGO sheets. Interestingly, "super-mesocrystals" formed by 3D oriented attachment of mesocrystals are also formed judging from the voided Sierpinski polyhedrons observed. Furthermore, the interior nanowire architecture of these mesocrystals can be kinetically controlled by careful variation of growth conditions. Owing to high specific surface area and improved conductivity, the rGO-Cu_2O mesocrystals achieved a higher sensitivity toward NO_2 at room temperature, surpassing the performance of standalone systems of Cu_2O nanowires networks and rGO sheets. The unique characteristics of rGO-Cu_2O mesocrystal point to its promising applications in ultrasensitive environmental sensors.

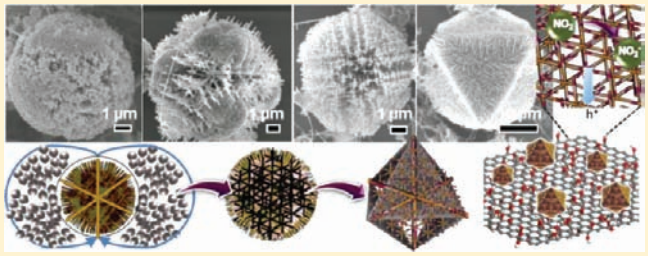

INTRODUCTION

Nanomaterials have become key components in sensing devices owing to their unique geometry and size- and shape-dependent characteristics.[1] The challenge to build industrially viable nanomaterial-based devices hinges on the ability to precisely control the spatial orientation and arrangement of nanoscale building blocks by bottom-up synthesis.[2,3] In particular, the synthesis of three-dimensional (3D) nanorod/nanowire superstructures with distinct structural and geometrical features such as arrays, networks, and hierarchical structures has gathered immense interest because of their inherent anisotropic nature and tunable spatial distribution, which give rise to extraordinary optical, magnetic, and electronic properties.[4,5] As opposed to conventional "ion-by-ion" crystal growth, the bioinspired nonclassical crystallization method birthed various self-organized mesoscale or microscale 3D superstructures made up of nonspherical subunits interspaced with organic additives, termed mesocrystals.[6] Some examples include the hexagonal prismatic seed crystal of fluorapatite in gelatin,[7,8] calcite,[9,10] aragonite,[11] vaterite,[12] copper oxalate,[13] hematite,[14] and ZnO.[15−17] However, despite the various proposed driving

Received: December 15, 2011
Published: February 14, 2012

   dx.doi.org/10.1021/ja211683m | *J. Am. Chem. Soc.* 2012, 134, 4905−4917

mechanisms such as surface tension, capillary effects, van der Waals force, electrostatic, steric repulsion, hydrophobic interactions, and directional dipolar interactions,[18−20] the formation mechanism of mesocrystals remains largely uncertain. In contrast to previous reports, where the structures of mesocrystals are comprised of densely stacked nanoparticles with low aspect ratio, self-organization of one-dimensional (1D) nanowires into 3D mesocrystal via a nonclassical crystallization approach offers more unique characteristics combining both 1D and collective physical properties. Nevertheless, it remains a challenge to organize interpenetrating 1D nanowires into ordered 3D superstructures with low filling factor because of the tendency toward parallel stacking of highly anisotropic shapes.[21]

The unique optical and electrical properties of cuprous oxide (Cu_2O) crystal, a p-type semiconductor, have ushered its successful integration in solar energy conversion, sensors, photocatalytic degradation, and coherent propagation of excitons.[22−25] The controlled synthesis of Cu_2O micro- and nanocrystals with a vast array of architectures including nanocubes, nanocages,[26] nanowires,[27] solid and hollow spheres, and polyhedrons, double tower-like tip nanostructures,[28] and multipods[29] had been achieved by a myriad of methods such as electrodeposition, thermal relaxation, sonochemical methods, vacuum evaporation, γ-irradiation and the liquid-phase reduction of a metal salt.[30−33] More recently, complex 3D structure like multipod Cu_2O frameworks and nanowire polyhedra have been reported.[29,34,35] However, the growth mechanism of these nanostructures is still confined within the framework of well-established "ion-by-ion" nanocrystal growth, where surfactants play a major role in the shape control of nanocrystal. Constructing higher order frameworks of Cu_2O crystals is far more complex and requires appropriate intercrystal connections to attain long-range ordered organizations of superstructures. Since the formation of Cu_2O mesocrystals has not been demonstrated possibly due to the intrinsic limitation of ionic precursors-based routes, it would be interesting to investigate if Cu_2O nanowire superstructures can be synthesized via a nonclassical crystallization route. More specifically, finding an appropriate modifier that can promote the formation of a polymeric matrix comprised of organic additives and amorphous nanoparticles at the initial phases (i.e., aggregation) is an important step in the formation of Cu_2O nanowire superstructures. Recent studies have demonstrated the novel physiochemical properties of GO as structural directing agent for formation of unconventional polymeric matrices for nanocomposites.[36−38] The quasi-2D structure of GO tethered with abundant functional groups imparts dual molecule-colloid properties to GO,[39] which elicit multivalent interaction with Cu^{2+} as well as polymer additive, both inducing and stabilizing the aggregation for subsequent particle-mediated crystallization.[40] Moreover, the reduced form of GO (rGO) is likely to conjugate with semiconductor superstructures under the hydrothermal growth condition and consequently enhance the physical and chemical properties of the composites for diverse applications.[41,42]

Motivated by this idea, we prepared rGO-conjugated Cu_2O nanowire mesocrystals (rGO-Cu_2O) using a one-pot hydrothermal treatment of copper(II) acetate in the presence of *o*-anisidine and GO. These mesocrystals possess distinct octahedral crystal faces and are made up of highly anisotropic nanowires as building blocks. Detailed studies on the time-dependent evolution of morphology and molecular dynamics are performed to elucidate the complex formation mechanism of such a nanowire mesocrystal. Intriguing voided Sierpinski polyhedrons are isolated and present strong evidence for the 3D-oriented attachment of individual octahedron to form a larger mesocrystal. A new perspective of nonclassical "nanoparticle-by-nanoparticle" growth is proposed, which we believe is a more efficient and plausible mechanism for the formation of such gigantic mesostructures. The role of GO in the mesoscale transformation of the thermodynamically metastable Cu_2O precursor phase to the final mesocrystals is assessed. In addition, a careful analysis of the effects of the type of organic additives, precursor concentration, and pH value on the nanowire architecture of mesocrystals was also conducted. We found that as the content of GO increased, the Cu_2O mesocrystals were gradually embedded on the large sheets of rGO to form 3D conducting networks. This rGO conjugated Cu_2O mesocrystal composite was evaluated as a NO_2 sensor because the synergistic combination of the interdendritic space within the mesocrystals and enhanced electronic conductivities provided by rGO are expected to enhance the sensitivity toward NO_2 gas sensing. The study aims to provide a model to adequately account for the formation mechanism of 3D self-organized mesocrystals consisting of highly anisotropic nanowires. This undoubtedly opens up new possibilities for mesocrystal-based nanodevice for various environmental sensing applications.

RESULTS AND DISCUSSION

Morphology and Characterization of Cu_2O Nanowire Mesocrystals and Its rGO Composites. The field-emission scanning electron microscopy (FESEM) images shown in Figure 1 (parts a and c−d) represent the typical Cu_2O nanowire mesocrystals synthesized in this work. The mesocrystals with octahedron morphologies and distinct triangular external faces are clearly evident with sizes ranging from 10 to 100 μm. Figure 1b shows the XRD patterns of the obtained mesocrystals where all diffraction peaks can be exclusively indexed to the cubic phase Cu_2O (JCPDS file No. 05−0667). An individual Cu_2O mesocrystal is comprised of branched nanowires with diameter ranging from 80 to 110 nm (Figure 1c,d). The surfaces of this octahedron mesocrystal are bounded with "crystal planes" of the {111} family, resembling the atomic or molecular species in the face centered cubic (FCC) crystal counterparts (see inset in Figure 1b). Interestingly, by superimposing a hand-drawn hexapod grid on the SEM image of the nanowire architecture (Figure 1d), it is clearly evident that the interior nanowire architecture can be thought of as an octahedron constructed by fractal growth of the hexapod. The appearance of such a hexapod subunit with six arms is plausible under diffusion-limited conditions,[43−45] which energetically favors branching along ⟨100⟩, ⟨001⟩, and ⟨010⟩ directions of the Cu_2O cubic crystal (labeled in the inset of Figure 1b). The defined directions of dendritic growth are a reflection of the symmetry of the underlying crystal lattice.[29] Repeated hexapod branching growth serves as a means to provide space for higher order organization of the Cu_2O mesocrystals, culminating in interpenetrating nanowires exhibiting 3-fold symmetry (from the (111) face) and a low filling factor. In addition, the absence of an extended continuous network of rGO at low GO concentration suggests that a small amount of GO (0.9 mg) suffices only to initiate the formation of Cu_2O nanowire mesocrystals. Only upon addition of 3 mg of GO, will the mesocrystals be interconnected via a rGO network

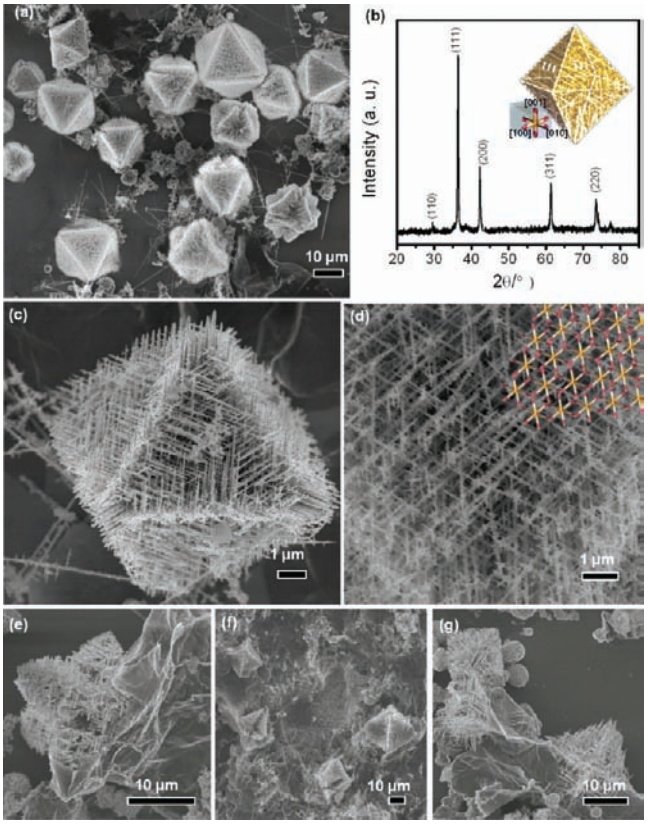

Figure 1. FESEM images of octahedron Cu_2O nanowire mesocrystals. (a) Overall product morphology of the octahedron Cu_2O nanowire mesocrystals. (b) XRD of the Cu_2O mesocrystals. The inset shows a schematic illustration of crystal structure of octahedron Cu_2O nanowire mesocrystal, with crystal orientations of hexapod branching shown. (c) An octahedron Cu_2O mesocrystal along the [111] view, and (d) interior morphology with overlaid hexapod grid. (e–g) SEM images of rGO-Cu_2O mesocystal composites of higher GO loading content.

as shown in Figure 1 (panels e–g). During the in situ crystal growth, GO forms complementary binding interactions with the Cu^{2+} ions,[40] and is subsequently reduced under hydrothermal conditions to rGO sheets to form an integral structural component of the assembled system. Since both components are in the size range of a few micrometers, the as-formed rGO-Cu_2O mesocrystals composite readily forms a continuous network spanning an area of at least 100 μm × 100 μm.

Transmission electron microscopy (TEM) is then employed to gain further insight into the crystallographic structure and composition of the nanowire mesocrystals. The low-magnification TEM image in Figure 2a provides an apt overview of the nanowire mesocrystal which consists of dendritic nanowires organized into a dense network, while an entire plane of dendritic nanowires is shown in Figure 2b. Selected area electron diffraction (SAED) patterns shown in the inset of Figure 2b reveal that the entire plane is single-crystalline. It is remarkable that the overall crystal symmetry is preserved for both branching and assembly throughout the growth process. Despite their complex branching manner, the hexapods/dendrites are crystallographically aligned with one another along some main crystallographic axes of Cu_2O. A fragment of the nanowire mesocrystal obtained by ultrasonication was investigated by TEM as well. As shown in Figure 2c,e, HRTEM images of both main stem and branch nanowire confirm their single-crystalline nature and well-resolved (001) and (110) lattice planes. HRTEM and the assignments of SAED (insets in Figure 2c,e) consistently indicate that the growth directions for stem and branch nanowire are [001] and [100], respectively. In accordance with the cubic crystallographic symmetry, [100]- and [010]-directed branches grow perpendicular to the [001]-directed stem nanowire. Although [010]-directed branches do not show up in TEM observation, the existence of [010]-directed branches could not be excluded due to both the cubic structure of Cu_2O and the nature of TEM analysis. The net result is that branched nanowires grow in a manner of hexapod orthogonal to one another, which is consistent with the observations from the SEM image. Furthermore, the tapered tip of nanowire is distinct from that of Cu_2O nanowires directly grown from the copper acetate precursor under similar condition,[27] indicating that the dissolution-recrystallization process, namely the Ostwald ripening mechanism, is responsible for the anisotropic growth of branched Cu_2O nanowires.[46] The TEM and HRTEM image of the rGO-Cu_2O mesocrystal composite obtained at high GO loading content in Figure 2f,g show that wrinkled rGO sheets cover the surface of the Cu_2O structures, as a result of folding and aggregation as GO sheets interact with Cu^{2+} in the aqueous solution.[40]

Several analytical techniques were further employed in sample characterization. The Raman spectra of rGO-Cu_2O mesocrystals composites reveal Raman bands at 219, 400, and 624 cm^{-1}, which can be assigned to, $2\Gamma_{12}^-$, $4\Gamma_{12}^-$, and $\Gamma_{15}^{-(2)}$ vibration modes of Cu_2O, respectively (Figure 3a).[47] After washing with *N*-methyl-2-pyrrolidone at 50 °C for 24 h to remove the polymeric materials, the D band of rGO at around 1323 cm^{-1} (attributed to the K-point phonons of A_{1g} symmetry) and the G band at around 1586 cm^{-1} (usually assigned to zone center phonons of $E_{2\,g}$ symmetry) are clearly visible (Figure 3a(ii)). The other Raman bands in spectrum (i) of Figure 3a are attributed to the capping polymer. Figure 3b shows the FTIR spectra of GO, Cu_2O, and Cu_2O-rGO composite and peak assignments are summarized in Figure 3c. The peaks at 1386, 1559, and 1506 cm^{-1} are attributed to the $-CH_3$-substituted group and the stretching vibration of the quinoid ring and the benzenoid ring of poly(*o*-anisidine), respectively. The bands at 1285 and 1248 cm^{-1} originate from the C–N and C–O stretching absorptions, respectively. The intense absorption band at 624 cm^{-1} is assigned to the copper–oxygen stretching vibration in the Cu_2O phase. These IR absorptions indicate that the poly(*o*-anisidine) is anchored on the surfaces of Cu_2O mesocrystals. More significantly, the new peaks at 1585 and 1654 cm^{-1} indicate N—H (amide II bands) and C═O (amide I band), which were the result of bonding between the −COOH groups of rGO and amine groups of poly(*o*-anisidine) for the rGO-Cu_2O composite. In addition to Raman spectroscopy, surface sensitive X-ray photoelectron spectroscopy (XPS) revealed more information about the chemical composition of the Cu_2O mesocrystals (Supporting Information, Figures S5 and S6). From the O 1s photoelectron spectrum, the peaks located at 530.7 and 532.0 eV can be assigned to the lattice oxygen of Cu_2O and the oxygen species of surface hydroxyl groups, respectively. The peak fitting of Cu $2p_{3/2}$ peak revealed a main peak at 932.5 eV corresponding to Cu_2O and a smaller peak at the high binding energy of 934.9 eV belonging to $Cu(OH)_2$. Auger spectroscopy carried out on the mesocrystals shows that kinetic energy of Cu LMM at 916.6 eV corresponds to the Cu_2O state (Supporting Information, Figure S8).

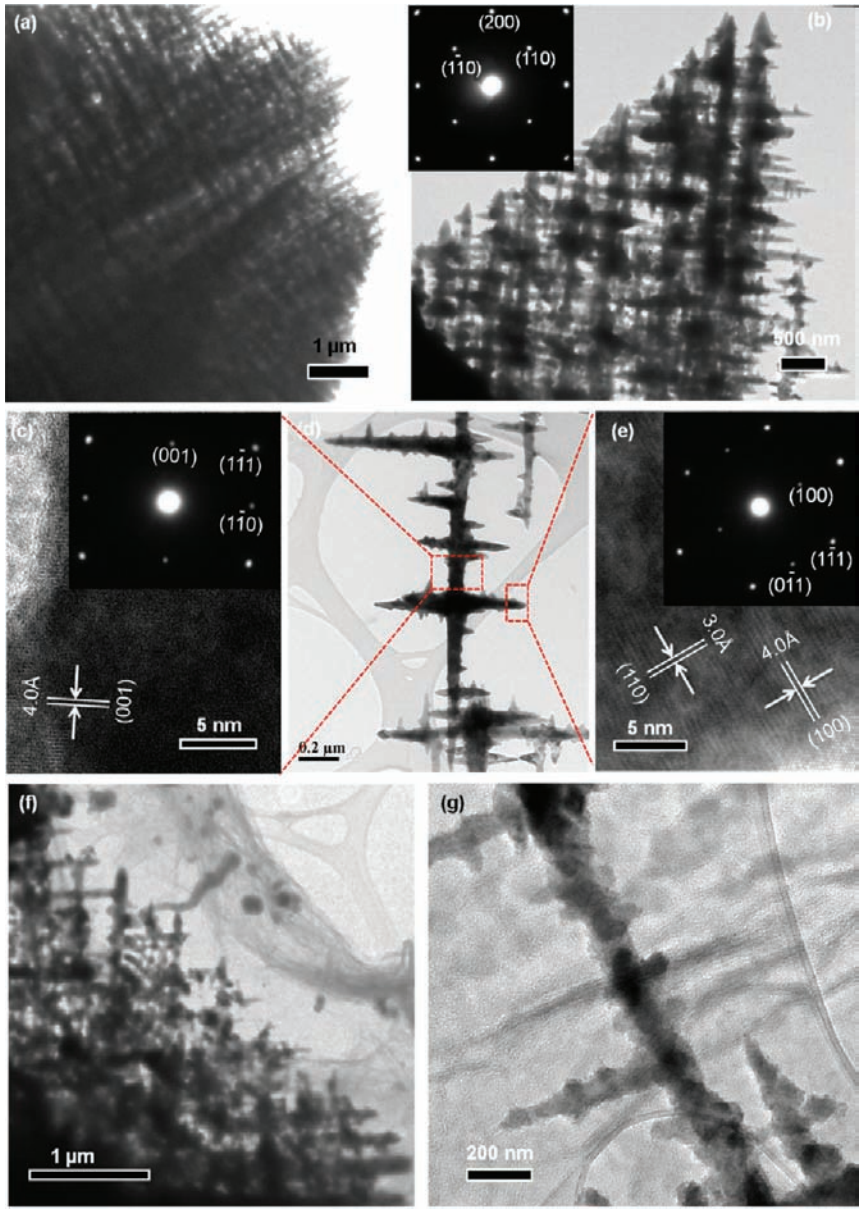

Figure 2. (a) Low-magnification TEM provides an overview of Cu_2O nanowire mesocrystal and (b) TEM image at the edge of the 3D mesocrystal. The inset shows SAED of the entire plane. (d) TEM image of a fragment of the nanowire mesocrystal. (c, e) HRTEM images of stem and branch nanowire indicated in panel d, respectively. The insets are the corresponding SAED patterns. (f) TEM and (g) HRTEM of image of rGO-Cu_2O mesocrystal composites of higher GO loading content.

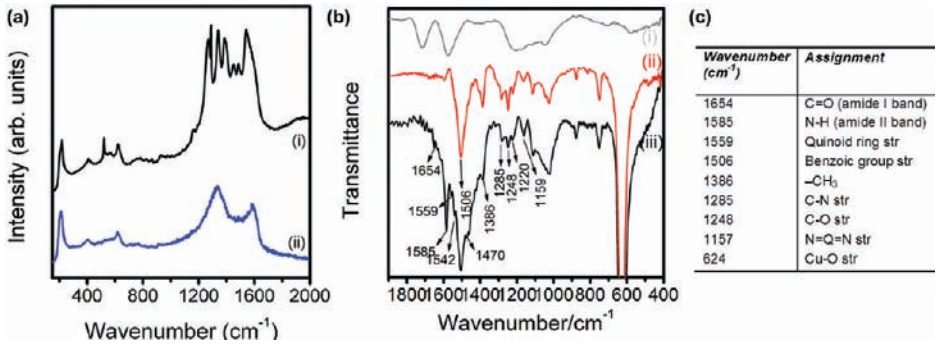

(c)

Wavenumber (cm^{-1})	Assignment
1654	C=O (amide I band)
1585	N-H (amide II band)
1559	Quinoid ring str
1506	Benzoic group str
1386	$-CH_3$
1285	C-N str
1248	C-O str
1157	N=O=N str
624	Cu-O str

Figure 3. (a) Raman spectra of (i) rGO-Cu_2O composites, and (ii) rGO-Cu_2O composites after washing with *N*-methyl-2-pyrrolidone at 50 °C for 24 h. (b) FTIR spectrum of (i) GO, (ii) Cu_2O, and (iii) rGO-Cu_2O in KBr pellet. (c) Assignment of FTIR absorption bands.

dx.doi.org/10.1021/ja211683m | *J. Am. Chem. Soc.* 2012, 134, 4905−4917

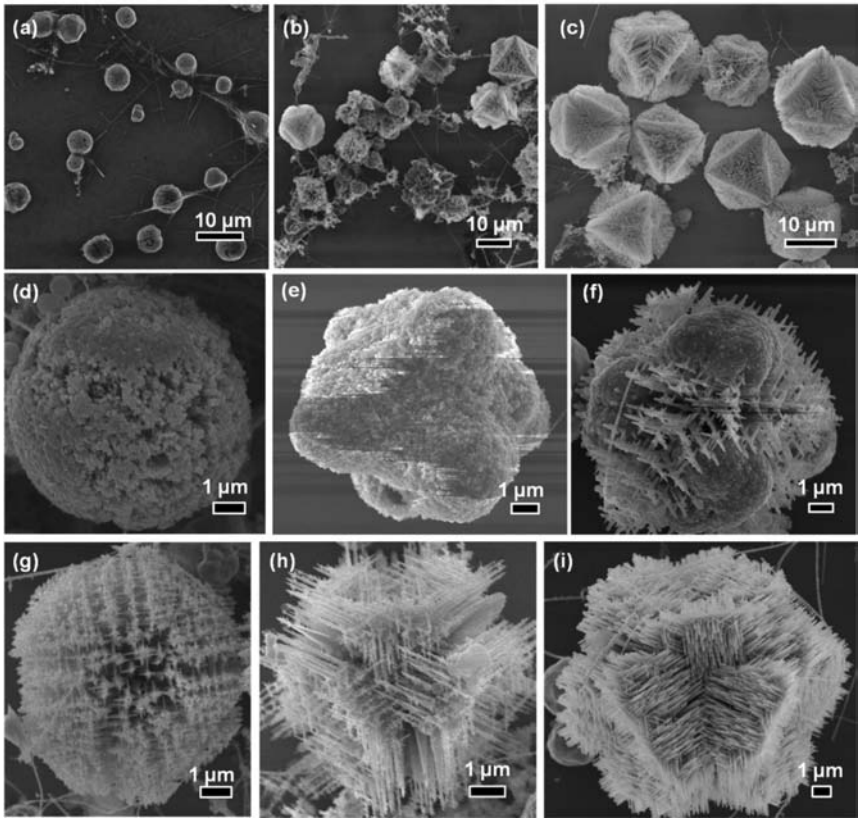

Figure 4. Morphology evolution of the precursors to the mesocrystals, as indicated by SEM images of the intermediates and products grown for reaction times of (a) 3, (b) 9, and (c) 15 h. (d–i) Representative SEM images illustrating the mesoscale transformation: (d) a typical spherulite; (e) spherulites formed an agglomerate of octahedral shape; (f, g) a spherulite partially evolved into the nanowire mesocrystal, revealing hierarchical structure; and (h, i) structure refinement into octahedron shape.

Morphology Evolution. For a complete understanding of the formation process of the Cu_2O nanowire mesocrystal, a systematic time-dependent morphology evolution study was conducted at 200 °C. Such time-resolved experiments are expected to provide important information to elucidate the underlying mechanisms. As shown in Figure 4a, at the early stage of the crystallization process (mesocrystal nucleation stage), fast nucleation resulted in the onset of the agglomeration of amorphous microspheres displaying roughened surfaces, while few free-standing Cu_2O nanowires are observed. After a growth time of 9 h, some small faceted mesocrystals begin to appear among the microspheres (Figure 4b), suggesting a mesoscale transformation from the "amorphous" spheres to "crystalline" mesocrystals.[41] At this stage, there remains a fraction of spherical mesocrystal intermediates yet to be fully transformed into faceted mesocrystals (a more detailed analysis is shown in the Supporting Information Figure S2). These eventually grow into large 3D mesocrystals with distinct octahedron shapes after 15 h of reaction (Figure 4c). It is noted that only nanowires are observed in the final product under identical reaction conditions in the absence of GO (Supporting Information, Figure S11a). By adding GO, both nanowire and amorphous microspheres are found at an intermediate reaction time (3–9 h). This leads us to a vital question: are the mesocrystals formed from the amorphous microspheres? To address this query, control experiments were conducted in which the nanowires formed at the early stage were retrieved from the precipitates after 5 h of growth and recombined with the supernatant before allowing them to grow further for 10 h. A similar procedure was repeated in a separate experiment whereby the nanowires were discarded and the precipitates were recombined with the supernatant for further growth. We found that only in the latter case would abundant mesocrystals form (Supporting Information, Figure S1). This provides a strong indication that the amorphous microspheres are temporarily stabilized intermediates, which eventually evolve into mesocrystals.

To understand the mesoscale transformation from amorphous microspheres to faceted mesocrystals, the morphologies of representative mescocrystal intermediates were captured at different stages (3–15 h) and shown in Figure 4d–i. The mesocrystal first takes the form of an undefined amorphous microsphere (Figure 4d,e). With increasing reaction time, the inner crystallized nanowires protruded from the organic matrix (Figure 4f). The amorphous microsphere then gradually evolved into spherical mesocrystal intermediates with hierarchical nanowire structure (Figure 4g). Such structures with curved surfaces are characteristic of a liquid and were similarly observed in the early intermediates during calcite crystallization.[48] More examples of the curved nanowire mesocrystal intermediate are shown in Figure S2(b–e) (Supporting Information). At the final stage, these hierarchical nanowire structures are transformed into faceted octahedral mesocrystals (Figure 4h,i). The morphological evolution is accompanied by corresponding changes in the composition of intermediates. Energy-dispersive X-ray spectroscopy (EDX) analyses of amorphous spheres and final mesocrystals showed that both

dx.doi.org/10.1021/ja211683m | J. Am. Chem. Soc. 2012, 134, 4905–4917

consist of C, O, and Cu (Figure S3). However, the C content in the mesocrystals was lower, indicating the decrease of polymeric content during the reaction. The Cu_2O mesocrystals and rGO-Cu_2O samples were also analyzed by thermal gravimetric analysis (TGA) (Supporting Information, Figure S4). The onset decomposition temperature of rGO-Cu_2O was between 200 and 300 °C. The rGO-Cu_2O mesocrystals show an approximate 15 wt % decrease in weight from 75 to 550 °C, which is consistent with the loss of poly(*o*-anisidine) and the decomposition of rGO. The reduced polymeric content during the structure evolution corroborates the results obtained from XPS. From the C−O content as shown in the O1s XPS spectrum (Supporting Information, Figure S6), the amount of polymer on the surface of Cu_2O mesocrystals is lower than that on the amorphous microspheres. These results clearly indicate the presence of polymeric materials within the interstitials of the mesocrystals and/or intermediates whose coverage on the surface of the mesostructures decreased as the reaction proceeded.

Atomistic Model for Mesoscale Transformation. Molecular dynamics (MD) simulations of the crystallization process were performed to understand the mesoscale transformation process with use of a prototypical FCC model system.[49] In particular, amorphous nanobuilding blocks were positioned, using crystallographic rules, at FCC lattice points within a cubic cell; MD was used to simulate their subsequent aggregation and crystallization. The resultant model structure was comprised of framework architecture with a complex arrangement of interconnecting cavities, channels and surfaces—commensurate with what we observe experimentally. Similar to using Miller indices to catalogue a crystal structure, it is possible to annotate the low index planes corresponding to a superlattice. Specifically, the atomistic models of a mesoporous structure, generated by positioning an FCC array of nanobuilding blocks in a cubic cell oriented along [100], and [111], together with the nanowire mesocrystals as viewed along [100], and [111] directions, are presented in Figure 5. On inspection, one can identify {100} and {111} planes, which correspond to the superlattice, in Figure 5, panels a−c and d−f, respectively. From the simulation results, we can infer that the self-organization of nanobuilding blocks into mesostructures is influenced by the "rules" of crystallography. During the mesoscale transformation, the particles are coaxed to assemble at specific locations for crystallization, under the effect of surface capping agents or dipole associated with the nanoparticles. As epitomized by our experimental data, the growth morphology of a superlattice can be considered as a hierarchical analogy to growth morphologies of crystals, where atoms attach at crystallographic positions on reactive surfaces and growth proceeds "atom-by-atom" during Ostwald ripening. Figure 5g, together with detailed analysis of the atomistic models, reveals that there exist synergistic interactions between the three hierarchical levels of structural complexity: (1) the crystal structure of the parent material, (2) microstructural features, and (3) superlattice structure; the latter relates to the internal topography or "shape" comprising the morphology of the cavities. The self-organizing process can be seen as an efficient self-amplifying scheme whereby controlled aggregation amplifies the mesocrystal morphology.

Formation Mechanism of Cu_2O Nanowire Mesocrystal. On the basis of the experimental and simulation results, the growth mechanism of Cu_2O nanowire mesocrystals is illustrated in Figure 6. The formation of the nanowire

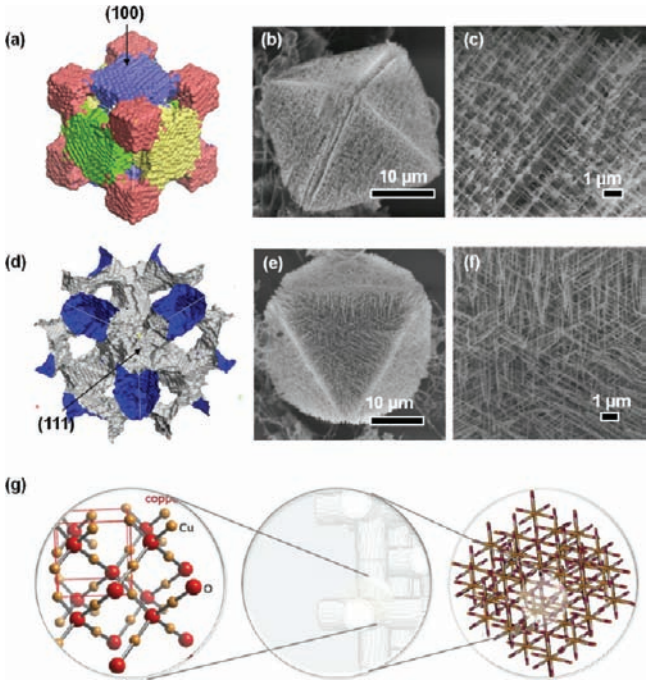

Figure 5. (a, d) Atomistic model obtained by positioning a FCC array of nanobuilding blocks into a cubic cell. SEM images of the structures when viewed along (b, c) [100] and (e, f) [111] directions, matches with the superlattice obtained from atomistic models. (g) Images depict three hierarchical levels of structural complexity comprising crystal structure (left), microstructure (middle), and superlattice structure (right).

mesocrystal is closely related to the introduction of GO into the reaction system. In the presence of only *o*-anisidine, the growth mechanism follows classical ion-by-ion growth and the anisotropic growth of nanowires is promoted by the selective adsorption of polymer onto certain Cu_2O crystal faces (Supporting Information, Figure S11a).[27] Upon addition of GO, a transition occurs in the particle structure and crystallization mechanism from single crystals to mesocrystals. GO, being essentially a single atomic sheet with its lateral dimension extending to the size of colloidal particles, renders it a unique material exhibiting molecule-colloid duality.[39] Figure 6a illustrates the "swollen gallery" that is supported by chemical and hydrogen bonds generated from interlinkage of the water molecules, Cu^{2+}, amine groups of *o*-anisidine, and the oxygen-containing groups on GO. Furthermore, the hydroxyl, carboxylic acid, ether epoxy functionalities decorating the basal planes and edges of GO may form oxo- or hydroxo-bridges with Cu^{+}/Cu^{2+} ions. The ζ potential of GO was measured to be −25 mV. After mixing with Cu^{2+}-*o*-anisidine complex, it shows a positive ζ potential of around +30 mV, suggesting the conjugation of Cu^{2+}-*o*-anisidine complex and GO. These favor the initial formation of colloidal solution as shown in Figure 6b. The strong association of the respective components due to the coordination and multidentate electrostatic interaction between Cu^{2+}, *o*-anisidine, and GO promotes supersaturation during the hydrolysis of copper acetate. A large amount of Cu_2O nanoparticles then nucleate and grow into small seed particles. To minimize the overall energy of the system, these seed particles tend to aggregate together to form amorphous microspheres as shown in Figure 6c. The *o*-anisidine-coordinated GO here acts as a polyelectrolyte, which temporarily stabilizes the amorphous Cu_2O

dx.doi.org/10.1021/ja211683m | *J. Am. Chem. Soc.* 2012, 134, 4905−4917

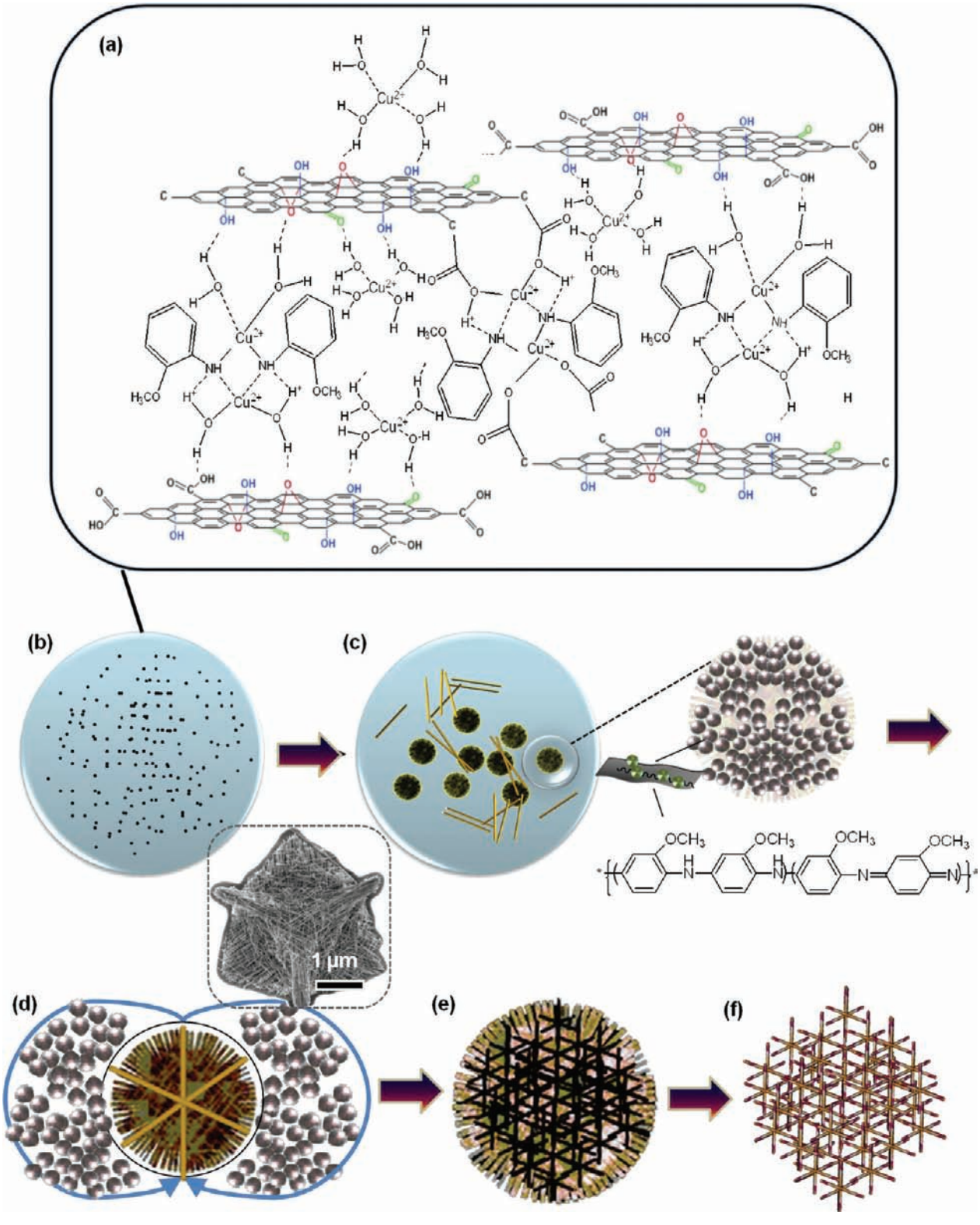

Figure 6. Schematic illustration of the Cu_2O crystallization process assisted by *o*-anisidine and GO. (a) Proposed association between Cu^{2+}, GO, and *o*-anisidine: multivalent bridging of GO with Cu^{2+} and *o*-anisidine, and hydrogen bonding between water molecules and Cu^{2+}. (b) Formation of polymer-stabilized colloidal solution of amorphous Cu_2O microspheres, the exact complexation processes as depicted in part a. (c) Aggregation and growth of amorphous microspheres, along with production of nanowires. Detailed view of the amorphous microsphere containing poly(*o*-anisidine), Cu_2O, and GO. (d) Formation of crystalline-like scaffold. Minimization of interactions between dipole fields of the crystalline rods led to three perpendicularly oriented rods with mutual 90° angles. The inset is a SEM of a collapsed droplet clearly showing the skeleton scaffold. (e) Magnified view featuring dendritic branching from the crystalline skeleton. A combination of dipole field, capping polymer, and crystal structure guide the orientation and nanowire branching growth. (f) Structure refinement by dissolution-recrystallization. Polymer diffuses outward from the core as monomer is depleted to form an octahedron nanowire mesocrystal.

dx.doi.org/10.1021/ja211683m | *J. Am. Chem. Soc.* 2012, 134, 4905−4917

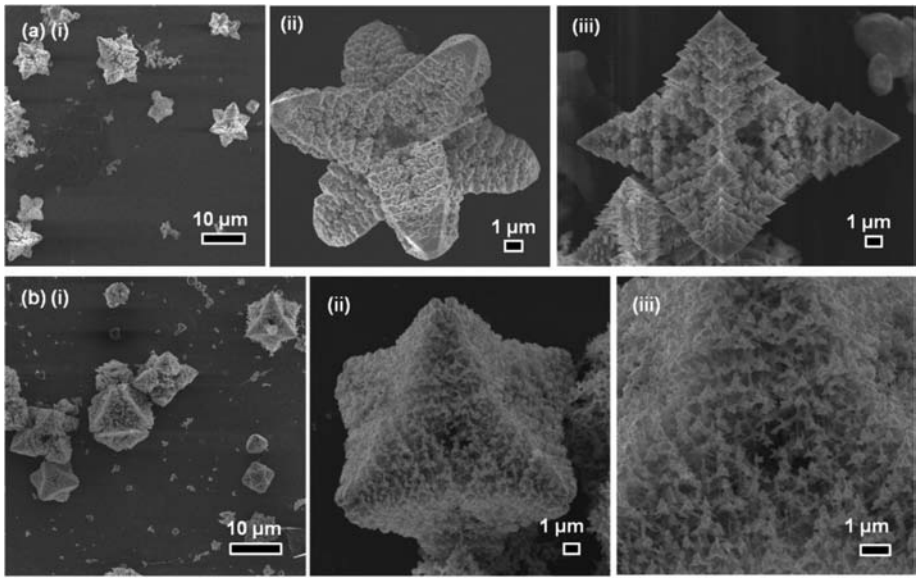

Figure 7. (a) Collected precipitate at 10 h, regrown for 11 h with supernatant with further addition of copper(II) acetate and 80 μL of *o*-anisidine. (b) Nanowire mesocrystals grown at pH 8.

precursor nanoparticles from tight and irreversible aggregation as a result of their amphipilicity.[50]

The stable and aggregated amorphous microspheres then undergo mesoscale transformation in the polymeric matrix (Figure 6c–f). The polymeric matrix comprising *o*-anisidine and GO plays an important role in the further morphogenesis of the mesostructures, and influences the orientation and morphology of nanocrystalline aggregates. During the oxidative polymerization reaction of *o*-anisidine and Cu^{2+} under hydrothermal conditions, it is plausible that the poly(*o*-anisidine) associated to GO may organize into distinctive geometric conformations, with the Cu^{+}/Cu^{2+} acting as linker and poly(*o*-anisidine) as strengthening agent as depicted in Figure 6c. Additionally, the densification of the matrix with reaction time, as *o*-anisidine is polymerized to longer chains of poly(*o*-anisidine), further decreases the apparent diffusion rate of ions and thus promotes diffusion-limited growth. For example, the increased nucleation rate driven by high local concentration of Cu^{2+} ions within the amorphous microspheres provides additional nucleation sites for nanowire branching. This can be deduced from the burrs on the fragmented nanowires in Figure 2d. Previous studies have shown that the morphology of crystals grown in gel matrix changes from polyhedrons into dendrites via skeletal forms as the gel density increased.[51] Under the matrix effects, self-organization and recrystallization of amorphous Cu_2O nanoparticles first leads to a crystalline-like scaffold composed of three poles within the microspherical droplets (Figure 6d). These poles with moderate mobility, which correspond to the skeletal forms at low gel density,[52] align in three orthogonal directions due to dipole repulsion and favor the formation of a hexapod structure. The SEM image of a collapsed droplet after removal of the capping polymer (inset in Figure 6d) clearly shows the thick pods consisting of the crystalline-like skeleton (the crystalline-like skeleton can also be seen joining the apexes of an early formed mesocrystal in Figure 4h and are also indicated in Figure 9). At this stage, the mesostructures are characterized by both "hard" and "soft" features—the crystalline skeleton exhibits the features of a solid while the soft condensed precursor accounts for the liquid-like character and the curved surfaces of some mesocrystal intermediates isolated at an early stage (Figures 4g and S2b–e, Supporting Information). As illustrated in Figure 6e, the skeletal structures gradually transform into dendritic structures governed by diffusion-limited growth. The hierarchical structure formed in the exposed portions of the amorphous microspheres (Figure 4f) proves that the morphogenesis occurs within the organic matrix that constitutes the amorphous microspheres. With time, Ostwald ripening occurs with the outward diffusion of poly(*o*-anisidine), which guide the growth of new branching nanowires structures with unique tapered ends (as seen earlier from the TEM characterization). The synergistic effects of the electric field generated by the crystalline-like skeleton and the dipole–dipole interaction under the effect of the capping polymer guides the alignment during growth of the dendritic hexapods. This results in the prevailing octahedral shape of the final mesocrystals bounded by {111} planes as shown in Figure 6f and accounts for the overall crystallographic alignment of the interpenetrating nanowires of hierarchical hexapods in the interior. Similar densely branching or spongy morphologies formed by nonclassical crystallization have been observed and attributed to diffusion-limited aggregation.[53] In summary, GO serves as a crystal growth modifier to promote growth of mesocrystals,[54] whereby its unique physiochemical properties play an important role in complexing with poly(*o*-anisidine) to form unconventional polymeric matrices for Cu_2O nuclei seeding and mesoscale transformation of the thermodynamically metastable Cu_2O precursor phase to the final mesocrystal consisting of oriented nanowire units.

Nonetheless, the elusive nature of the complete structure of GO poses a great challenge in verifying the role of functional groups on the mesocrystal growth.[55] For instance, differences in the density of −COOH and −OH groups on GO exist within a single batch, earlier exfoliated sheets were more oxidized than the later exfoliated sheet. To identify the role of functional groups on the nanowire mesocrystal growth, GO was replaced with molecules with different carboxylic acid groups. Perylene-3,4,9,10-tetracarboxylic dianhydride (PTCDA), which has a conjugated aromatic planar structure with four carboxylic acid groups, thus represents an analogue of GO, but with a more

dx.doi.org/10.1021/ja211683m | *J. Am. Chem. Soc.* 2012, 134, 4905–4917

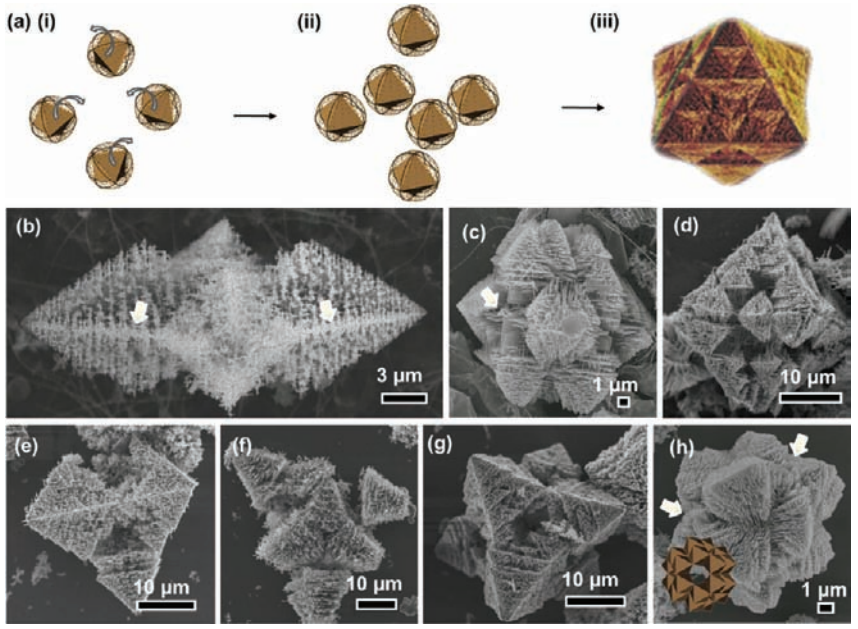

Figure 8. Second tier growth via oriented attachment. (a) Schematic illustration of 3D oriented attachment of Cu_2O nanowire mesocrystal. (i, ii) Particle rotation for alignment, (iii) followed by self-organization of oriented building blocks into larger supermesocrystals via 3D oriented attachment. (b) Aggregation of four octahedron units into a partially formed mesocrystal, crystalline-like skeleton is prominent. (c) An example of a truncated octahedron and (d) Sierpinski octahedron formed by oriented attachment of building units, leaving behind prominent voids. (e) (110) view of partially formed octahedron, with voids resembling Sierpinski polyhedron (f) Process of formation of stellated octahedron is captured as one of the arms is attached to the body. (g) Voided Sierpinski stellated octahedron. (h) Quartet octahedron. Arrows indicate crystalline-like skeleton in the shape of a cross. The inset shows an illustration of a quartet octahedron.

precise chemical structure. Figure S9a,b Supporting Information shows that nanowire mesocrystals can also be produced by using PTCDA as the additive. This result reveals that the −COOH groups on GO may be a key functional group for the mesocrystal growth. Additional comparison experiments using a variety of carboxylic acid additives indicate that only multicarboxylic acids (PTCDA and 4,4′,4″,4‴-(porphine-5,10,15,20-tetrayl)tetrakis(benzoic acid)) promote the formation of well-defined octahedral nanowire mesocrystals (Supporting Information, Figure S9). Simple carboxylic acids like tartaric acid produce spearhead terminated framework structures together with abundant spherical agglomerates (Supporting Information, Figure S9e,f), while acetic acid produced branched hierarchical structures resembling natural foliage (Supporting Information, Figure S9g,h); both do not yield octahedron nanowire mesocrystals. These support our hypothesis that the multivalent amphiphilic GO leverages the morphogenesis of octahedron nanowire mesocrystals with greater ease than small carboxylic acids by appropriate adjustment of the physiochemical forces.[38] The fact that other multicarboxylic acids can induce similar mesocrystal formation is an important observation, implying that the GO, PTCDA, and porphyrin-COOH additives share a common characteristic of possessing carboxylic acid groups which may serve a similar role to biomimetic crystallization using acidic polypeptides.[56] Other factors such as the supersaturation and the pH value also affect the growth of mesocrystals. Hence a control experiment was performed to investigate the effect of precursor concentration and supersaturation on the crystal growth. After 5 h of mesocrystal growth, the reaction was quenched and cooled then more copper(II) acetate and *o*-anisidine were added to the reaction mixture and the reaction was continued for 10 h. An increase in supersaturation within the organic matrix changes the final morphology from the octahedral nanowire mesocrystals to stellated octahedrons consisting of large hexapods crystallites stacked together as shown in Figure 7a. Although such mesocrystals can be identified as being built up by hexapod-like crystallites, nanowire subunits cannot be distinguished. It is likely that with increased polymeric content and dissolved Cu^{2+} ions, the growth rate is greatly increased and disrupts the regular branching growth, resulting in the loss of 1D characteristic of the subunit. Our results are consistent with the observation that the shape of Cu_2O nanostructures can be controlled under different kinetic conditions as dictated by precursor concentration according to a diffusion-limited progressive growth model.[57] An increase in pH produces a similar effect as an increase in supersaturation. Stellated octahedrons are the prevalent product under a high pH condition (pH 8) due to the increase in growth rates (Figure 7b(i,ii)) by altering the dissolution-recrystallization process.[35] The increased growth rate is also evident from the observation of "melted" or coalesced appearance in the fundamental unit of stellated octahedron mesocrystal (Figure 7b(iii)). These imply that the mesocrystal is susceptible to the changes in the chemical environment, and therefore may be more a kinetic, metastable intermediate than a thermodynamically stable product.

Oriented Attachment. In addition to mesoscale transformation, the self-organization of small mesocrystals into larger mesocrystals via 3D oriented attachment is also observed in the later growth stage (beyond 12 h). The formation of such complex structures with a good level of control over their shape and size has to be a result of oriented attachment. Figure 8a schematically illustrates the formation process of "supermesocrystal" by oriented attachment. The capping polymer not only stabilizes the mesocrystal but also participates in

dx.doi.org/10.1021/ja211683m | *J. Am. Chem. Soc.* 2012, 134, 4905−4917

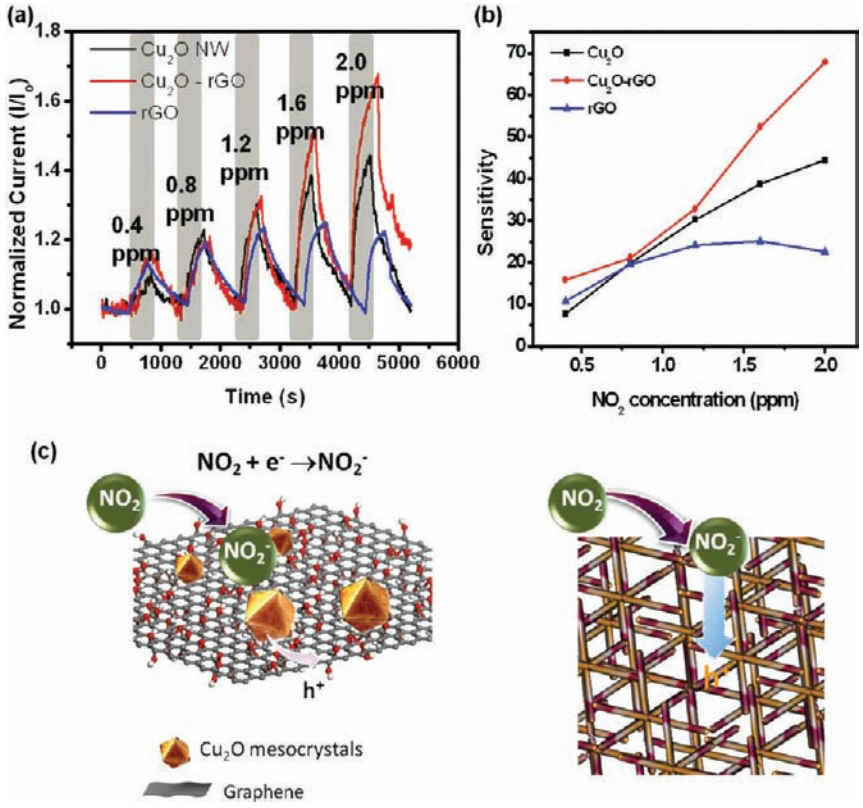

Figure 9. (a) Dynamic response of Cu_2O NW, rGO-Cu_2O, and rGO devices under increasing NO_2 exposure. (b) The sensitivities of NO_2 sensor for the three devices. (c) Schematic for mechanism of NO_2 sensing of rGO-Cu_2O.

kinetic control of oriented attachment. The adsorption of in situ formed poly(*o*-anisidine) results in charged mesocrystals. The nonspherical shape of the mesocrystals lead to anisotropic particle polarization, hence electrostatic repulsion potential will be at a maximum when crystallographic planes of mesocrystals approach each other.[58] Such electrostatic interaction is believed to mutually align anisotropic building units prior to collision (Figure 8a(i,ii)). However, reduction in the amount of polymeric content with reaction time causes unstable early formed small mesocrystals to fuse together into a larger mesocrystal at the edges in an effort to reduce the total surface energy (Figure 8a(iii)).[59,60] Similar self-organization of small inorganic building blocks mediated by absorbed polymer molecules had been observed in the formation of Sierpinski octahedral calcite mesocrystals.[61] As shown in Figure 8b–h, the 3D oriented attachment is substantiated by the formation of voids/defects in intermediate structures. Figure 8b shows a structure possibly formed by a head-to-head fusion of four octahedron building blocks in the (001) plane. A high contrast plane from which the dendritic nanowires grow out from, which appears as a "cross" when viewed from the (100) direction, is likely to be the self-organized crystalline-like skeleton. Voids reminiscent of the Sierpinski polyhedrons were created within the octahedron assembly due to the rapid attachment of the outer building blocks, as can be seen in Figure 8c,d,e,g (also Supporting Information, Figure S10c). This is a fascinating discovery because it implies that partial overlap of the plane just at the edges of the octahedrons can lead to a successful oriented attachment. A similar instance of joining of edges of planes can be witnessed in the construction of 3D SnO_2 hollow octahedral.[62] A stellated-octahedron structure is captured in the process of formation as the side arms are attached to piece the final form in Figure 8f. Figure 8h shows a quartet octahedron made up of prominent octahedral building blocks and arrows indicate the presence of crystalline scaffold. The "Sierpinski" voids imply that "edge-to-edge" or "head-to-head" connections are preferred over "face-to-face" connection, indeed caused by the repulsion between facing crystallographic planes as the octahedral building blocks approach each other. In addition to the voids left behind in the newly formed supermesocrystal, confluence of highly ordered structures with similar planes at an angle results in incoherent interfaces and interfacial defects to relieve strain at the interface (Supporting Information, Figure S10a,b,f). In the extreme case of accommodating interfacial strain, overlapping twin crystals and irregularly faceted shapes may arise (Supporting Information, Figure S10d,e). Further edge sharing growth and hexapod branching growth by the process of dissolution-recrystallization may help to fill up the voids and refine the structure. The occurrence of oriented attachment opens up possibilities of 3D self-amplification of mesocrystals to construct macroscopic architectures for fundamental studies and future applications.

Gas Sensing. NO_2 detection is of paramount importance in explosives detection as it is a decomposition product of many explosive formulations and improvised explosive devices. It is also very useful in monitoring pollutants emitted by industrial and recycling processes. Therefore, we evaluated the NO_2 gas-sensing ability of the rGO-Cu_2O mesocrystal composite and compared its performance with those of rGO and Cu_2O nanowires. The SEM images for Cu_2O nanowires and rGO samples are shown in Figure S11 (Supporting Information). The dynamic response of Cu_2O nanowires, Cu_2O-rGO composite, and rGO sensor for room temperature detection

dx.doi.org/10.1021/ja211683m | *J. Am. Chem. Soc.* 2012, 134, 4905–4917

of increasing concentration of NO_2 gas (0.4−2.0 ppm) is shown in Figure 9a. The sensitivities of the three devices are plotted against gas concentration (Figure 9b). During the exposure of NO_2 the sensitivities of all three devices increases with increasing gas concentration due to the similar p-type nature of both Cu_2O and rGO. At 2.0 ppm, the sensitivities of rGO, Cu_2O nanowire, and rGO-Cu_2O mesocrystal composite were 22.5%, 44.5%, and 67.8%, respectively. The calculated limits of detection (LOD) are 81, 64, and 82 ppb for Cu_2O, rGO-Cu_2O, and rGO, respectively. Hitherto, to the best of our knowledge, this is the first demonstration of NO_2 gas sensing by metal oxide, where a low LOD is achieved at room temperature. Previous studies on NO/NO_2 sensing by Cu_2O nanostructures indicate that good sensitivities can only be achieved at elevated temperatures (~150 °C).[63] In addition, because metal oxide requires activation of oxygen ion in order to create a significant surface depletion layer to alternate the electric field upon gas adsorption,[64] the diffusion of gas molecules to the active surface becomes a limiting factor for detection at a higher concentration. Such a performance limiting factor is eliminated for rGO-Cu_2O mesocrystal composite because rGO nanosheets do not require oxygen activation. Therefore, with an augmentation of active surface area, the rGO-Cu_2O mesocrystal composite displays a significant enhancement in detection at concentrations higher than 1.2 ppm as compared to that of Cu_2O nanowires.

The sensing mechanism for rGO-Cu_2O composites can be described as the charge doping by gas species that modifies the conductivity. When in contact with the oxidizing NO_2 gas, the gas molecule receives an electron from the "activated" surface oxygen ion and promotes the hole conductivity in the Cu_2O device (Figure 9c). Since rGO synthesized by chemical modification is not pristine graphene but graphene decorated with electron-withdrawing oxygen functionalities, rGO possesses p-type semiconductor characteristics.[65] The p-type semiconducting behavior of rGO-Cu_2O is apparent from the drain-source current (I_{ds})−drain-source voltage (V_{ds}) curves at different gate voltages (V_g) (Supporting Information, Figure S12), in which the conductance decreases with increasing V_g. The interaction with an oxidizing gas such as NO_2 withdraws an electron from rGO, thus increasing the hole conductance.[66] Since the operation of such sensors involves adsorption/desorption phenomena and reactions at the interface, the surface accessibility of nanocrystals is crucial to maintain their high sensitivity.[67] The 2D stacking and lack of hierarchical hollow microstructure limited the sensitivity of the nanowires or rGO because the analyte gas molecules could only interact with a thin layer of sensing elements. On the contrary, rGO-Cu_2O composite offers a much larger surface accessibility, increased conductivity, and hence higher sensitivity toward NO_2 gas, owing to the highly oriented and porous interpenetrating nanowire structure coupled to the rGO sheets. In particular, the planar 2D GO sheets create an extensive 3D network that enhances interconnectivity among the crystals to boost sensor performance, which other multicarboxylic additives cannot achieve.

CONCLUSIONS

In summary, the rGO-conjugated octahedral Cu_2O nanowire-mesocrystals have been successfully fabricated through a nonclassical cystallization process in the presence of *o*-anisidine and GO under hydrothermal conditions. The obtained Cu_2O mesocrystal with eight {111} equivalent faces possesses a high nanoscale intracrystal porosity as a result of highly oriented interpenetrating nanowires architecture and ultrathin nanowire building blocks with high aspect ratio (>100), a morphology that is in stark contrast to conventional mesocrystals. The experimental evidence from time-dependent characterization, isolation of various mesocrystal intermediates, and the results of MD simulations suggests that these nanowire mesocrystals are formed by means of particle-mediated aggregation under diffusion-limited condition, subsequently undergoing a meso-scale transformation from amorphous microspheres to intermediate spherical structure, and finally to the nanowire mesocrystals with a high degree of orientation via Ostwald ripening. GO plays an essential role in the transition of growth mechanism from conventional ion-by-ion growth to non-classical particle-mediated aggregation by promoting the formation of amorphous microsphere at the early stage. Additional comparison experiments with a variety of carboxylic acid additives like PTCDA identify the significant contribution of multicarboxylic groups of GO in leveraging the morphogenesis of nanowire mesocrystals, which also extend the possibilities of control of mesocrystals morphogenesis in the future. With increased GO loading content, the porous 3D Cu_2O mesocrystals were embedded on the large sheets of rGO to form integrated rGO conjugated-Cu_2O hybrid architecture. The observation of voided Sierpinski polyhedrons corroborates 3D oriented attachment of mesocrystals to form "super-mesocrystals". The interior architecture of mesocrystals can be kinetically controlled by adjusting the supersaturation level, pH, and type of organic additives. The interplay and synergy of high surface area-to-volume ratio of the 3D nanowire mesocrystals and enhanced conductivity of the rGO network endows the composite with improved NO_2 sensing performance over the constituent counterparts, attaining an unprecedented detection limit of 64 ppb at room temperature. The mesocrystals and its rGO composites developed in the current work not only provide an excellent model to study the 3D self-organization of 1D functional semiconductor nanowire but also open up new possibilities for designing mesocrystal-based nanodevices for various sensing applications.

METHODS

Preparation of rGO-Conjugated Cu_2O Nanowire Mesocrystals. Copper(II) acetate, *o*-anisidine (>99%), acetic acid (≥99.7%), 4,4′,4″,4‴-(porphine-5,10,15,20-tetrayl)tetrakis(benzoic acid) (porphyrin-COOH) (Dye content, 75%), perylene-3,4,9,10-tetracarboxylic dianhydride (PTCDA) (97%), and L-(+)-tartaric acid (≥99.5%) were purchased from Sigma-Aldrich and used as-received without further purification. GO was prepared by the Hummers method.[68] In a typical synthesis, 0.2 g of copper(II) acetate and 0.3 mL of 3 mg/mL GO were dissolved in 40 mL of deionized water, followed by the addition of 80 μL of *o*-anisidine. The mixture was stirred for 5 min to form an olive-green solution. The solution was transferred into a 50 mL Teflon-lined stainless autoclave and maintained at 200 °C for 15 h. The final pH of the supernatant was 4.0. For crystals formed at higher pH, the pH of the precursor mixture was adjusted from pH 7 to pH 8 with 1 M KOH. The autoclave was cooled naturally to room temperature. The sediments were isolated by decanting the supernatant colloidal polymer solution, and then thoroughly washed with ethanol several times. Nanowires coexisted with the mesocrystals in the products were removed by centrifuging at 1250 rpm for 1 min. The final product was dried at 60 °C in an oven for subsequent characterization. The composite of rGO-Cu_2O mesocrystal with a high rGO content was prepared by using similar procedures while 1 mL of 3 mg/mL GO was added into the reaction solution.

Synthesis of Cu_2O Nanowires and rGO. Cu_2O nanowires were synthesized by using the same conditions with 10 h of reaction. Nanowires coexisted with the mesocrystals in the products and could be separated by collecting the supernatant after centrifuging at 1250 rpm for 1 min. The products were similarly collected by centrifugation and repeatedly washed with ethanol. For comparison, GO nanosheets were synthesized, characterized, and hydrothermally reduced to rGO and employed as a sensing material for NO_2.

Materials Characterization. The crystalline structure of the as-prepared Cu_2O crystals was characterized with X-ray diffraction (XRD, Bruker-AXS, Cu Kα (1.542 Å) radiation). Cu_2O morphologies were characterized by field emission scanning electron microscopy (FESEM, JEOL JSM-6700F) and transmission electron microscopy (TEM, JEOL JEM-3010). Raman spectra were measured by the Renishaw Invia system with a 532 nm excitation line. The thermal behavior of the as-prepared Cu_2O-rGO composites was characterized with thermogravimetric analysis (TGA) in a TA Instruments SDT 2960. In each experiment, about 10 mg of the sample was heated at a rate of 10 °C/min from 30 to 1000 °C with flowing nitrogen as a stream at 100 mL/min. Absorption FTIR spectroscopy of the Cu_2O and rGO-Cu_2O composites was performed with a Varian 3100 Excalibur Series FTIR spectrometer with a nominal resolution of 2 cm^{-1}. Sixty four accumulative scans were collected.

Generation of Atomistic Models. Nanoparticles of MgO, comprised of 25200 atoms, were cleaved from the parent bulk material. The nanoparticles were then amorphised by heating, under molecular dynamics (MD) simulation, to 4000 K. The molten nanoparticles were then posited at FCC sites and MD simulation performed at 1200 K to enable the nanoparticles to crystallize and self-assemble. The unit cell was comprised of four nanoparticles (101 000 atoms). Finally, the system was cooled to 0 K by using MD and the model structures analyzed by using molecular graphical techniques. Further details pertaining to this method can be found in ref 49. MgO, rather than Cu_2O, nanobuilding blocks were considered to reduce the complexity of the simulations; both MgO and Cu_2O comprise metal atoms, which occupy FCC positions.

Gas Sensing Measurement. The sensors were fabricated by drop casting Cu_2O-rGO on prepatterned electrodes. Evaluation of the sensing capability of each material was carried out in a homemade setup, using Keithley S4200 with two probe configurations. The target gas, NO_2 (NOX, Singapore, max 2 ppm), was passed to the chamber through a manual mass flow meter to control the gas flow rate. Current was normalized and plotted against the time. Sensitivity is defined as $S = [(I_{gas} - I_o)/I_o] \times 100\%$, where I_{gas} is the current detected under target gas exposure and I_o is the current detected under N_2 exposure.

■ ASSOCIATED CONTENT

Supporting Information

TGA, XPS, EDX, and Auger results for Cu_2O mesocrystals and intermediates and additional SEM images showing mesocrystal intermediates, mesostructures obtained with various carboxylic acid additives, defects in mesocrystals, SEM and TEM images of Cu_2O nanowires and rGO sheets. This material is available free of charge via the Internet at http://pubs.acs.org.

■ AUTHOR INFORMATION

Corresponding Author

nanofhm@gmail.com; physowch@nus.edu.sg

Notes

The authors declare no competing financial interest.

■ ACKNOWLEDGMENTS

This work is supported by the Singapore National Research Foundation under CRP Award No. NRF-CRP-4-2008-03 and National Natural Science Foundation of China (NSFC) under grant No. 21006079. We acknowledge the help of Assoc. Prof Tok Eng Soon and Dr. Zhang Zheng for the XPS characterization.

■ REFERENCES

(1) Jun, Y. W.; Seo, J. W.; Oh, S. J.; Cheon, J. *Coord. Chem. Rev.* **2005**, *249*, 1766−1775.
(2) Martin, C. R. *Science* **1994**, *266*, 1961−1966.
(3) Bierman, M. J.; Lau, Y. K. A.; Kvit, A. V.; Schmitt, A. L.; Jin, S. *Science* **2008**, *320*, 1060−1063.
(4) Lee, J. M.; Choung, J. W.; Yi, J.; Lee, D. H.; Samal, M.; Yi, D. K.; Lee, C. H.; Yi, G. C.; Paik, U.; Rogers, J. A.; Park, W. I. *Nano Lett.* **2010**, *10*, 2783−2788.
(5) Wang, D.; Luo, H.; Kou, R.; Gil, M. P.; Xiao, S.; Golub, V. O.; Yang, Z.; Brinker, C. J.; Lu, Y. F. *Angew. Chem., Int. Ed.* **2004**, *43*, 6169−6173.
(6) Xu, A. W.; Ma, Y. R.; Cölfen, H. *J. Mater. Chem.* **2007**, *17*, 415−449.
(7) Xu, S.; Qin, Y.; Xu, C.; Wei, Y. G.; Yang, R. S.; Wang, Z. L. *Nat. Nanotechnol.* **2010**, *5*, 366−373.
(8) Simon, P.; Zahn, D.; Lichte, H.; Kniep, R. *Angew. Chem., Int. Ed.* **2006**, *45*, 1911−1915.
(9) Kulak, A. N.; Iddon, P.; Li, Y. T.; Armes, S. P.; Cölfen, H.; Paris, O.; Wilson, R. M.; Meldrum, F. C. *J. Am. Chem. Soc.* **2007**, *129*, 3729−3736.
(10) Wang, T. X.; Cölfen, H.; Antonietti, M. *J. Am. Chem. Soc.* **2005**, *127*, 3246−3247.
(11) Nassif, N.; Gehrke, N.; Pinna, N.; Shirshova, N.; Tauer, K.; Antonietti, M.; Cölfen, H. *Angew. Chem., Int. Ed.* **2005**, *44*, 6004−6009.
(12) Xu, A. W.; Antonietti, M.; Cölfen, H.; Fang, Y. P. *Adv. Funct. Mater.* **2006**, *16*, 903−908.
(13) Jongen, N.; Bowen, P.; Lemaitre, J.; Valmalette, J. C.; Hofmann, H. *J. Colloid Interface Sci.* **2000**, *226*, 189−198.
(14) Shindo, D.; Park, G. S.; Waseda, Y.; Sugimoto, T. *J. Colloid Interface Sci.* **1994**, *168*, 478−484.
(15) Liu, Z.; Wen, X. D.; Wu, X. L.; Gao, Y. J.; Chen, H. T.; Zhu, J.; Chu, P. K. *J. Am. Chem. Soc.* **2009**, *131*, 9405−9412.
(16) Ye, F.; Peng, Y.; Chen, G. Y.; Deng, B.; Xu, A. W. *J. Phys. Chem. C* **2009**, *113*, 10407−10415.
(17) Peng, Y.; Xu, A. W.; Deng, B.; Antonietti, M.; Cölfen, H. *J. Phys. Chem. B* **2006**, *110*, 2988−2993.
(18) Quan, Z. W.; Fang, J. Y. *Nano Today* **2010**, *5*, 390−411.
(19) Yu, S. H.; Antonietti, M.; Cölfen, H.; Hartmann, J. *Nano Lett.* **2003**, *3*, 379.
(20) Tian, Z. R.; Voigt, J. A.; Liu, J.; Mckenzie, B.; Mcdermott, M. J. *J. Am. Chem. Soc.* **2002**, *124*, 12954−12955.
(21) Zhou, W. Z.; Cao, J.; Liu, W. C.; Stoyanov, S. *Angew. Chem., Int. Ed.* **2009**, *48*, 378−381.
(22) Briskman, R. N. *Sol. Energy Mater. Sol. Cells* **1992**, *27*, 361−368.
(23) Zheng, Z. K.; Huang, B. B.; Wang, Z. Y.; Guo, M.; Qin, X. Y.; Zhang, X. Y.; Wang, P.; Dai, Y. *J. Phys. Chem. C* **2009**, *113*, 14448−14453.
(24) Sahoo, S.; Husale, S.; Colwill, B.; Lu, T. M.; Nayak, S.; Ajayan, P. M. *ACS Nano* **2009**, *3*, 3935−3944.
(25) Snoke, D. *Science* **1996**, *273*, 1351−1352.
(26) Kuo, C. H.; Huang, M. H. *J. Am. Chem. Soc.* **2008**, *130*, 12815−12820.
(27) Tan, Y. W.; Xue, X. Y.; Peng, Q.; Zhao, H.; Wang, T. H.; Li, Y. D. *Nano Lett.* **2007**, *7*, 3723−3728.
(28) Zhang, H. W.; Zhang, X.; Li, H. Y.; Qu, Z. K.; Fan, S.; Ji, M. Y. *Cryst. Growth Des.* **2007**, *7*, 820−824.
(29) Chang, Y.; Zeng, H. C. *Cryst. Growth Des.* **2004**, *4*, 273−278.
(30) Lu, C.; Qi, L.; Yang, J.; Wang, X.; Zhang, D.; Xie, J.; Ma, J. *Adv. Mater.* **2005**, *17*, 2562−2567.
(31) Yin, M.; Wu, C. K.; Lou, Y.; Burda, C.; Koberstein, J. T.; Zhu, Y. *J. Am. Chem. Soc.* **2005**, *127*, 9506−9511.
(32) Siegfried, M. J.; Choi, K. S. *J. Am. Chem. Soc.* **2006**, *128*, 10356−10357.

(33) Liu, H. R.; Miao, W. F.; Yang, S.; Zhang, Z. M.; Chen, J. F. *Cryst. Growth Des.* **2009**, *9*, 1733−1740.
(34) Shi, J.; Li, J.; Huang, X.; Tan, Y. W. *Nano Res.* **2011**, *4*, 448−459.
(35) Xu, J. S.; Xue, D. F. *Acta Mater.* **2007**, *55*, 2397−2406.
(36) Petit, C.; Bandosz, T. J. *Adv. Mater.* **2009**, *21*, 4753.
(37) Guo, F.; Kim, F.; Han, T. H.; Shenoy, V. B.; Huang, J. X.; Hurt, R. H. *ACS Nano* **2011**, *5*, 8019−8025.
(38) Jasuja, K.; Berry, V. *ACS Nano* **2009**, *3*, 2358−2366.
(39) Kim, J. Y.; Cote, L. J.; Kim, F.; Yuan, W.; Shull, K. R.; Huang, J. X. *J. Am. Chem. Soc.* **2010**, *132*, 8180−8186.
(40) Yang, S. T.; Chang, Y. L.; Wang, H. F.; Liu, G. B.; Chen, S.; Wang, Y. W.; Liu, Y. F.; Cao, A. N. *J. Colloid Interface Sci.* **2010**, *351*, 122−127.
(41) Cölfen, H.; Mann, S. *Angew. Chem., Int Ed.* **2003**, *42*, 2350−2365.
(42) Liang, Y. Y.; Li, Y. G.; Wang, H. L.; Zhou, J. G.; Wang, J.; Regier, T.; Dai, H. J. *Nat Mater.* **2011**, *10*, 780−786.
(43) Mann, S. *Nature* **1993**, *365*, 499−505.
(44) Imai, H.; Oaki, Y. *Angew. Chem., Int. Ed.* **2004**, *43*, 1363−1368.
(45) Halsey, T. C. *Phys. Rev. Lett.* **1994**, *72*, 1228−1231.
(46) Wang, W. Z.; Xu, C. K.; Wang, G. H.; Liu, Y. K.; Zheng, C. L. *Adv. Mater.* **2002**, *14*, 837−840.
(47) Ivanda, M.; Waasmaier, D.; Endriss, A.; Ihringer, J.; Kirfel, A.; Kiefer, W. *J. Raman Spectrosc.* **1997**, *28*, 487−493.
(48) Song, R. Q.; Cölfen, H.; Xu, A. W.; Hartmann, J.; Antonietti, M. *ACS Nano* **2009**, *3*, 1966−1978.
(49) Sayle, D. C.; Seal, S.; Wang, Z. W.; Mangili, B. C.; Price, D. W.; Karakoti, A. S.; Kuchibhatla, S. V. T. N.; Hao, Q.; Mobus, G.; Xu, X. J.; Sayle, T. X. T. *ACS Nano* **2008**, *2*, 1237−1251.
(50) Kim, J. W.; Lee, D.; Shum, H. C.; Weitz, D. A. *Adv. Mater.* **2008**, *20*, 3239−3243.
(51) Oaki, Y.; Imai, H. *Cryst. Growth Des.* **2003**, *3*, 711−716.
(52) He, J.; Zhang, Q.; Gupta, S.; Emrick, T.; Russell, T. R.; Thiyagarajan, P. *Small* **2007**, *3*, 1214−1217.
(53) Oaki, K.; Imai, H. *Angew. Chem., Int. Ed.* **2005**, *44*, 6571−6575.
(54) Mann, S.; Archibald, D. D.; Didymus, J. M.; Douglas, T.; Heywood, B. R.; Meldrum, F. C.; Reeves, N. J. *Science* **1993**, *261*, 1286−1292.
(55) Gao, W.; Alemany, L. B.; Ci, L. J.; Ajayan, P. M. *Nat. Chem.* **2009**, *1*, 403−408.
(56) Homeijer, S. J.; Barrett, R. A.; Gower, L. B. *Cryst. Growth Des.* **2010**, *10*, 1040−1052.
(57) Radi, A.; Pradhan, D.; Sohn, Y.; Leung, K. T. *ACS Nano* **2010**, *4*, 1553−1560.
(58) Wang, Y.; Chen, G.; Yang, M. X.; Silber, G.; Xing, S. X.; Tan, L. H.; Wang, F.; Feng, Y. H.; Liu, X. G.; Li, S. Z.; Chen, H. Y. *Nat. Commun.* **2010**, 1.
(59) Wohlrab, S.; Pinna, N.; Antonietti, M.; Cölfen, H. *Chem.—Eur. J.* **2005**, *11*, 2903−2913.
(60) Wang, T. X.; Antonietti, M.; Cölfen, H. *Chem.—Eur. J.* **2006**, *12*, 5722−5730.
(61) Xu, A. W.; Antonietti, M.; Yu, S. H.; Cölfen, H. *Adv. Mater.* **2008**, *20*, 1333−1338.
(62) Yang, H. G.; Zeng, H. C. *Angew. Chem., Int. Ed.* **2004**, *43*, 5930−5933.
(63) Shishiyanu, S. T.; Shishiyanu, T. S.; Lupan, O. I. *Sens. Actuators, B* **2006**, *113*, 468−476.
(64) Barsan, N.; Weimar, U. *J. Electroceram.* **2001**, *7*, 143−167.
(65) Fowler, J. D.; Allen, M. J.; Tung, V. C.; Yang, Y.; Kaner, R. B.; Weiller, B. H. *ACS Nano* **2009**, *3*, 301−306.
(66) Joshi, R. K.; Gomez, H.; Alvi, F.; Kumar, A. *J. Phys. Chem. C* **2010**, *114*, 6610−6613.
(67) Pinna, N.; Neri, G.; Antonietti, M.; Niederberger, M. *Angew. Chem., Int. Ed.* **2004**, *43*, 4345−4349.
(68) Hummers, W.; Offeman, R. *J. Am. Chem. Soc.* **1958**, *80*, 1339.